Journal of Sound and Vibration (2001) **248**(4), 635–652
doi:10.1006/jsvi.2001.3807, available online at http://www.idealibrary.com on IDEAL®

SEISMOGRAMS OF MOVING TRAINS: COMPARISON OF THEORY AND MEASUREMENTS

A. DITZEL, G. C. HERMAN AND G. G. DRIJKONINGEN

Centre for Technical Geoscience, Delft University of Technology, Mekelweg 4, 2628 CD Delft, The Netherlands. E-mails: A.Ditzel@math.tudelft.nl; G.C.Herman@math.tudelft.nl; G.G.Drijkoningen@ta.tudelft.nl

(*Received* 26 *October* 2000, *and in final form* 6 *April* 2001)

High-speed trains can generate strong vibrations that propagate away from the track. In this paper, an efficient method is presented to calculate the displacements, generated by a moving train. It is based on an integral representation of the response and is computed numerically in the slowness domain. By expressing the field in terms of reflection and transmission properties of the layers, the effects of stratification are taken into account. Field measurements with vertical geophones have been carried out and a comparison is made with predictions from the theoretical model. The predicted vibrations show good agreement with the experimental response; both the computed and measured results clearly show the Doppler effect. Surface waves, generated by oscillating trains, can be observed at large distances from the track, even if the train speed is lower than the speed of the surface waves.

1. INTRODUCTION

Intensive ground vibrations can be generated by high-speed trains and can cause annoyance to the public living or working in the vicinity of the track. Particularly in soft-soil regions, where the train speed may approach or even exceed the surface-wave speed, a high vibration level can occur. In recent years, the generation of vibrations due to high-speed trains has received considerable attention. Several methods have been developed to predict the vibration level.

Krylov [1] investigates the effect of track dynamics on the vibrations due to high-speed trains. The vibrations generated by the bending track are computed with the aid of a Green function formulation and its farfield asymptotic behaviour in an elastic half-space. For trains travelling with a lower speed than the Rayleigh wave in the half-space, the presence of sleepers appears to be essential for the generation of vibrations. An increased effect on the level of ground vibration occurs for trains travelling with trans-Rayleigh speed.

Herman [2] formulated the problem of vibrations generated by moving high-speed trains in terms of a scalar integral-equation formulation. It was found that heterogeneities near the track contribute to the vibrations at relatively large distances from the track, even if the train speed is less than the subsurface wave speed.

Luco and Apsel [3] presented a method to obtain the dynamic three-dimensional response of a layered half-space for an arbitrarily buried source. They made use of the frequency-domain formulation based on representing the complete response in terms of semi-infinite integrals over the horizontal wavenumber. De Barros and Luco [4] made use of this procedure to determine the steady state response of a multi-layered visco-elastic half-space for a buried source that moves with constant velocity along a line. Numerical

0022-460X/01/490635 + 18 $35.00/0

results for the displacement and the stress field are given for both surface and buried loads moving with various subsonic and supersonic speeds.

Sheng *et al.* [5, 6] investigated the vibrations of a harmonic load moving over a layered ground. The track, including rails, rail pads, sleepers and ballast, was modelled by means of a multi-component mass–spring system. The ground was modelled as a structure of three-dimensional visco-elastic layers overlying either a half-space or a rigid foundation. From several calculations, it was shown that propagating waves are produced for loads travelling with a velocity higher than the critical wave speed. It is shown that both constant and harmonic loads contribute significantly to the vibrations generated by the train.

In the present paper, the response of a layered half-space to a moving (high-speed) train is investigated. The train is modelled by means of a vertical, oscillating point source, moving over the horizontally layered, three-dimensional elastic half-space with a traction-free surface. As a moving source can be considered as a superposition of point sources with appropriate phases, the generated wavefield can be calculated by expressing it as an integral representation, which can be done efficiently in the slowness domain (slowness is defined as wavenumber divided by frequency). Further, to take the effects of layering into account, the field is expressed in terms of transmission and reflection properties of the layers. Finally, the field is transformed back to the spatial domain and, subsequently, to the time domain by use of an inverse Fourier transform.

The present paper is closely related to the papers by, e.g., de Barros and Luco [4] and Sheng *et al.* [5, 6], in which models based on wavenumber theory are used. However, the methods presented in references [4–6] make use of the propagator matrix method of Thomson and Haskell [7, 8], and the approach in this paper is based on the more recent approach of Kennett [9] instead. This method avoids exponentially growing terms which correspond to the evanescent field and is reported to have better properties as far as numerical stability and accuracy is concerned (see reference [9, p. 135]). This is especially important in the case of thick layers. It is noted that Sheng *et al.* [5], showed that the numerical difficulties can also be avoided with a modification of the Thomson and Haskell method.

Results from a multi-receiver field experiment, which was performed in order to measure seismograms due to moving trains, are presented. The experimental set-up consisted of two receiver lines, one perpendicular and one parallel to a railway track, each consisting of 24 geophones and recording vertical particle velocity. First, the signal due to a small explosive charge was recorded, from which an estimate of the soil parameters could be made. These soil parameters have been used as input parameters for the model. Several train passages have been recorded and some of these results are shown in this paper. A comparison is made between the experimental and theoretical results. The effect of train speed and oscillatory behaviour of the train on the level of vibrations is investigated. The Doppler shift and the other features occurring in the field data are investigated. The predictions of the vibrations due to moving trains show a good qualitative agreement with the recordings from the field experiment.

2. FORMULATION OF THE PROBLEM

2.1. MOVING SOURCES

A semi-infinite elastic medium is considered, consisting of N homogeneous and horizontal layers overlying a homogeneous elastic half-space. Each of the media is characterized by its density ρ_n and by the compressional and shear wave velocities α_n and β_n

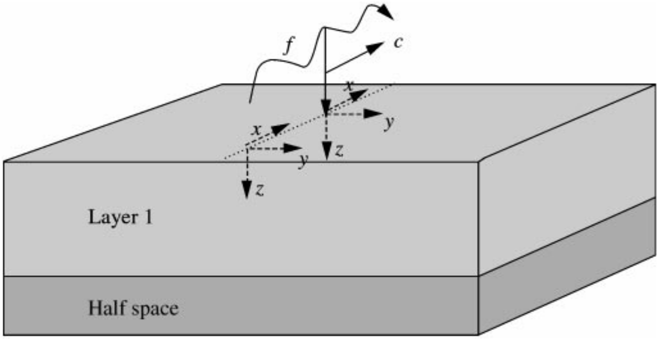

Figure 1. Geometry of the problem. The train is modelled by an oscillating point force, with strength f, moving with constant velocity c over a layered medium. The medium consists of N homogeneous layers, overlying a homogeneous half-space. Here, (x, y, z) is the stationary frame of reference and (x', y, z) is the frame moving with the train.

$(n = 1, N + 1)$. The wave velocities are assumed to be complex (with $\mathrm{Re}\{\alpha_n, \beta_n\} \geqslant 0$ and $\mathrm{Im}\{\alpha_n, \beta_n\} \leqslant 0$) in order to take dissipation of the media into account. The surface of the medium is taken to be traction-free and the radiation condition is imposed in the underlying half-space. Figure 1 shows a schematic model of the geometry.

For each of the N layers, the equation of motion and the constitutive relation hold:

$$\partial_i \tau_{ij}(\mathbf{x}) + \omega^2 \rho_n u_j(\mathbf{x}) = -f_j(\mathbf{x}), \tag{1}$$

$$\tau_{ij}(\mathbf{x}) = \lambda_n \delta_{ij} \partial_k u_k(\mathbf{x}) + 2\mu_n \partial_i u_j(\mathbf{x}) \quad \text{for } z_{n-1} < z < z_n, \quad n = 1, \quad N + 1, \tag{2}$$

where u is the displacement and τ the stress tensor. Furthermore, z_n is the interface below the nth layer, z_0 is the free surface co-ordinate and $\mathbf{x}$ a position vector, given by $\mathbf{x} = x\mathbf{i}_1 + y\mathbf{i}_2 + z\mathbf{i}_3$ and ω is the angular frequency of the Fourier transform. In equation (1), f_j is the force model of the train, which moves with a constant velocity c in the x direction. In equation (2), λ_n and μ_n are Lamé coefficients.

Excited by irregularities in the track and the wheels of its wagons, the train can show an oscillatory behaviour. In the train co-ordinate system (x', y, z), a force is then observed which is of the form

$$f_j(x', y, z, t) = a_j \delta(x') \delta(y) \delta(z) \cos(\omega_c t) \tag{3}$$

or

$$f_j(x', y, z, t) = f_j^G(x', y, z; 0, 0, 0) \cos(\omega_c t), \tag{4}$$

where ω_c is the resonant frequency of the train and δ is the one-dimensional Dirac delta function. The strength and the direction of the force are denoted by a_j. In equation (4), f_j^G denotes a three-dimensional point force, observed at position (x', y, z) and exerted at position $(0, 0, 0)$. To obtain the force in the stationary frame of reference, the co-ordinate transform $x' = x - ct$ is used. Subsequently, the Fourier transform is applied. The moving source in the stationary co-ordinate system (x, y, z) can now be written as

$$f_j(x, y, z, \omega) = W(\omega) a_j \int_t \mathrm{d}t \, \delta(x - ct) \delta(y) \delta(z) \cos(\omega_c t) \mathrm{e}^{\mathrm{j}\omega t} \tag{5}$$

$$= (W(\omega)/c) a_j \, \delta(y) \, \delta(z) \, \mathrm{e}^{\mathrm{j}(\omega/c)x} \cos((\omega_c/c)x), \tag{6}$$

where (x, y, z) is the position vector of the receiver in the stationary frame of reference. By means of the window function $W(\omega)$, the transfer function of the total acquisition system (source wavelet, receiver transfer function and recording instrument transfer function) is taken into account.

The moving point force can be expressed as a superposition of single point sources, each of which has a different phase due to the speed and the oscillatory movement of the train

$$f_j(\mathbf{x}) = \frac{W(\omega)}{c}\int_{x_s} \mathrm{d}x\, a_j \delta(x - x_s)\,\delta(y)\,\delta(z) \mathrm{e}^{\mathrm{j}(\omega/c)x_s}\cos((\omega_c/c)x_s), \tag{7}$$

or

$$f_j(\mathbf{x}) = \frac{W(\omega)}{c}\int_{x_s} \mathrm{d}x_s f_j^G(x, y, z; x_s, 0, 0)\mathrm{e}^{\mathrm{j}(\omega/c)x_s}\cos((\omega_c/c)x_s), \tag{8}$$

where the ω-dependence of f_j has been omitted for convenience. As the system is assumed to be linear, the wavefield generated by the moving source is obtained by superposition of the wavefields generated by a single point source with the result

$$u_j(\mathbf{x}) = \frac{W(\omega)}{c}\int_{x_s} \mathrm{d}x_s u_j^G(x, y, z; \mathbf{x}_s)\mathrm{e}^{\mathrm{j}(\omega/c)x_s}\cos((\omega_c/c)x_s), \tag{9}$$

with u_j^G representing the Green solution, a state of disturbance, for a point force f_j^G, exerted at position $\mathbf{x}_s = (x_s, 0, 0)$ and observed at position $\mathbf{x} = (x, y, z)$. For convenience, in equation (9), the ω-dependence of u_j and u_j^G has been omitted. By using a complex notation for the cosine term and using the shift invariance of the Green solution, the displacement can be written as

$$u_j(\mathbf{x}) = \frac{W(\omega)}{2c}\mathrm{e}^{\mathrm{j}(\omega+\omega_c/c)x}\int_{x_s} \mathrm{d}x_s \mathrm{e}^{-\mathrm{j}(\omega+\omega_c/c)(x-x_s)} u_j^G(x - x_s, y, z; 0)$$

$$+ \text{ same expression with } \{\omega_c \to -\omega_c\}, \tag{10}$$

which in turn can be written as

$$u_j(\mathbf{x}) = \frac{W(\omega)}{2c}\mathrm{e}^{\mathrm{j}\omega p_1^+ x}\int_{\tilde{x}} \mathrm{d}\tilde{x}\mathrm{e}^{-\mathrm{j}\omega p_1^+ \tilde{x}} u_j^G(\tilde{x}, y, z; \mathbf{0}) + \{p_1^+ \to p_1^-\}, \tag{11}$$

with $p_1^\pm = (\omega \pm \omega_c/\omega)/c$, the horizontal slowness for the x-co-ordinate, and $\tilde{x} = x - x_s$. The integral in equation (11) is recognized as a slowness transform with respect to the x-co-ordinate. By using the inverse slowness transform for the y-co-ordinate, an expression in terms of the horizontal slownesses is obtained:

$$u_j(\mathbf{x}) = \frac{\omega W(\omega)}{4\pi c}\mathrm{e}^{\mathrm{j}\omega p_1^+ x}\int_{p_2} \mathrm{d}p_2 \mathrm{e}^{\mathrm{j}\omega p_2 y}\tilde{u}_j^G(p_1^+, p_2, z; \mathbf{0})$$

$$+ \text{ same expression with } \{p_1^+ \to p_1^-\}, \tag{12}$$

where $p_1^\pm = (1 \pm \omega_c/\omega)/c$.

In equation (12), $\tilde{u}_j^G$ denotes the slowness transform of the Green solution u_j^G with respect to the spatial horizontal co-ordinates. The slowness transform with respect to the x-co-ordinate can be calculated analytically, which leaves the response in the frequency domain as an integral with respect to the slowness in the y direction. This integral is computed numerically. In this way, the generated wavefield can be calculated efficiently.

2.2. GREEN SOLUTION OF A LAYERED MEDIUM

In order to calculate the response of the soil to the moving and oscillating load, a representation of the Green solution in the slowness domain, $\tilde{u}_j^G$, for a layered medium has to be obtained. Kennett [9] presented a derivation of the response of plane-layered media to a point source. Because of the axial symmetry of the problem, Kennett poses the problem in terms of cylindrical co-ordinates. To obtain a formulation of the Green solution in equation (12) for plane-layered media in terms of slownesses, a method similar to that which Kennett presents can be followed, although in the present formulation, the load is moving in a fixed horizontal direction, and axial symmetry is lost. Therefore, use is made of Cartesian co-ordinates and thus the present method becomes slightly different. For this reason, all expressions necessary for the computations are presented in Appendix A. For the description of the solution method for the Green solution in the slowness domain, $\tilde{u}_j^G$, the reader is referred to this appendix, where the resulting expression for $\tilde{u}_j^G$ can be found in equation (A.17).

2.3. RESPONSE IN THE SPACE–TIME DOMAIN

The response of the layered ground to the moving, oscillatory, vertical load, can be calculated by substituting the results of the Green solution in terms of slownesses, $\tilde{u}_j^G$ (see equation (A.17)), into equation (12). For plane-layered media, all expressions and matrices occurring in the method described above are algebraic in the slowness domain. Subsequently, equation (12) is algebraic and thus the vibrations can be determined by numerical computation of the integral over slowness p_2, taking possible singularities properly into account by including attenuation. This is done by making the Lamé coefficients complex, with $\mathrm{Re}\{\lambda_n, \mu_n\} \geqslant 0$ and $\mathrm{Im}\{\lambda_n, \mu_n\} \leqslant 0$. Numerical integration results in an expression in the space–frequency domain. Finally, the inverse Fourier transform is performed, in order to obtain the wavefield in the space–time domain.

3. COMPARISON OF EXPERIMENTAL AND COMPUTATIONAL RESULTS

In order to observe seismograms due to moving trains, a pilot experiment has been performed. Two receiver lines, each consisting of 24 vertical geophones, were laid out, one parallel to the railway track (further referred to as the parallel line) and the other perpendicular (perpendicular line) (see Figure 2). The geophones were placed with a 2·5 m spacing and recorded vertical particle velocity. Use was made of 10 Hz geophones, with a 12 dB per octave damping factor below 10 Hz and a recording cut-off frequency of 1 Hz. Several of trains passages have been recorded. In order to obtain an estimate of the different soil parameters at the test site, the response of the soil to a small explosive charge has been recorded as well. In Figure 3(a) this response is displayed. In this seismogram, the vertical particle velocity has been plotted as a function of horizontal distance and time.

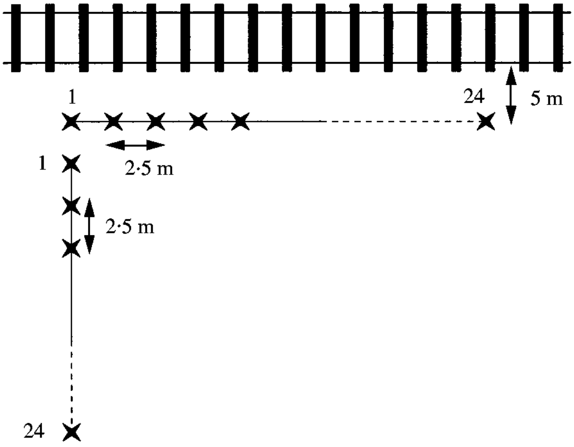

Figure 2. Top view of the experimental set-up. Twenty-four receivers have been laid out (parallel to the track) and 24 perpendicular to the track. Receiver spacing is 2·5 m.

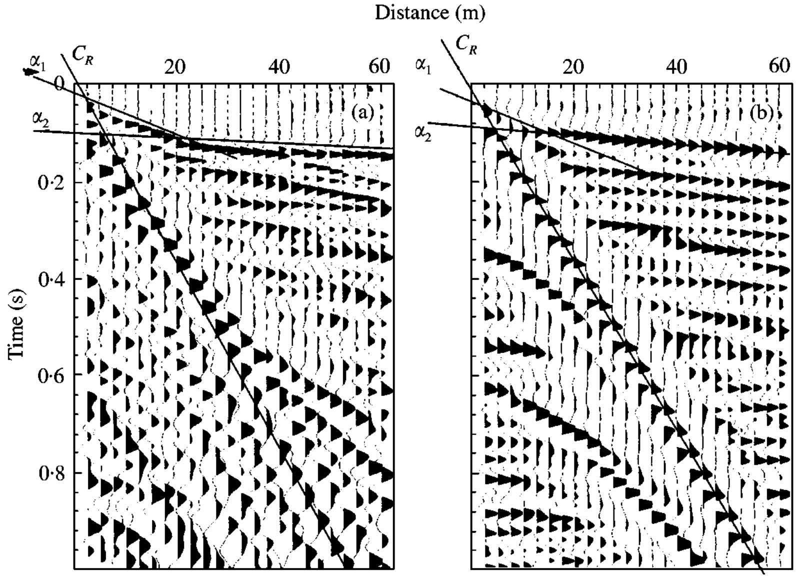

Figure 3. Response of the soil to an active, non-moving source (a), and the simulated response (b). In (a) three events can be clearly distinguished: the direct and the head wave, indicated by α_1 and α_2, respectively, and the Rayleigh wave (c_R).

Three different events can be distinguished clearly in Figure 3(a) (indicated by α_1, α_2 and c_R), of which one is the refraction (α_2). Therefore, the simple assumption is made that the subsurface can be modelled by one layer, overlying a half-space. An estimate of the thickness of this layer has been found. For this purpose, the wave speeds of the direct wave and the refracted compressional wave are to be estimated, which can be done by determining the slopes of the lines connecting the phase arrivals in the seismogram. Figure 4 shows a close-up of two different recordings; the difference being the position of the explosive charge. The two different source positions during the experiment are indicated by the flags at the top margin. Comparison of the velocities in both shot gathers in Figure 4

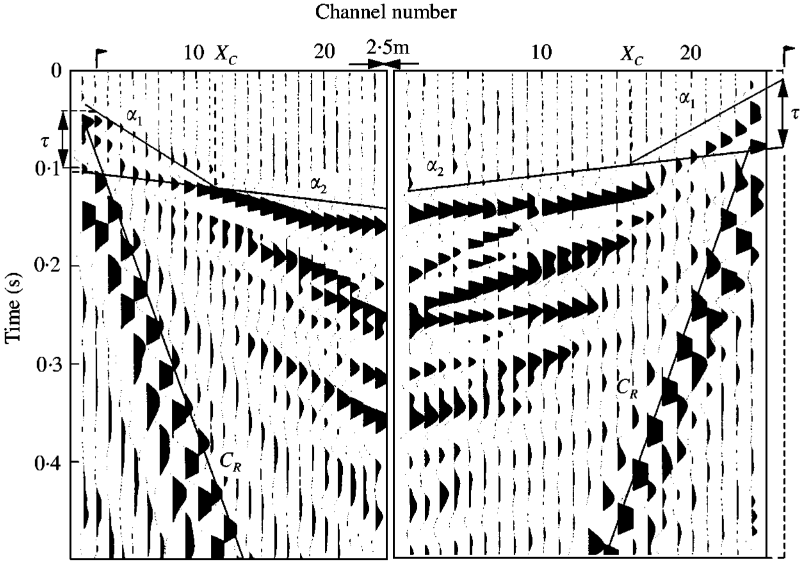

Figure 4. Close-up of the response of the soil to an explosive charge, for two shot positions (indicated by the flag). Three different events can be clearly distinguished. The Rayleigh wave in the top layer, c_R, travels with a speed of 57 m/s. The compressional wave speeds, for the top layer, α_1, and the half-space, α_2, are 325 and 1650 m/s respectively; τ denotes the intercept time for the compressional wave arrivals and x_c is the critical distance from which the layer depth can be estimated.

confirms the assumption that the subsurface can be interpreted as a horizontal one-layer model. At large offsets, the refracted wave travels with the speed of the P-wave in the second layer, i.e., the homogeneous half-space for this model. The direct wave is the P-wave in the top layer. Thus, an estimate for α_1 and α_2 can be made. Now, the thickness of the top layer can be estimated by means of the relation

$$h = (x_c/2)\sqrt{(\alpha_2 - \alpha_1)/(\alpha_2 + \alpha_1)}, \tag{13}$$

where x_c is the critical distance as indicated in Figure 4. From the slopes, a P-wave speed of 325 m/s in the top layer (indicated by α_1 in Figure 3(a)) and 1650 m/s in the half-space (α_2) is obtained. The critical distance is about 22·5 m, suggesting a layer thickness of about 9·3 m. For further details on seismic data processing, the reader is referred to reference [10].

The shear wave speeds in the top layer and the underlying half-space are estimated from the usual values for the ratio between P- and S-waves for the Dutch soil. For soft soil, this ratio (i.e., α/β) lies between 4 and 7, and it decreases for increasing P-wave speeds. Taking this ratio as 5·5 in the top layer and 4·2 in the underlying half-space, shear wave speeds of 60 and 380 m/s are obtained.

The speed of the shear wave in the top layer can also be estimated by the speed of the Rayleigh wave, which carries most of the energy and is clearly visible in the seismogram (c_R in Figure 3(a)). The speed of the Rayleigh wave is about 57 m/s, which gives the reasonable suggestion that the shear wave is 5% faster than the Rayleigh wave.

A depth of 9·3 m is too deep for the water table in average Dutch soil conditions, but locally it may be deeper. The first layer, with the estimated thickness of about 9·3 m, is interpreted to be above the water table or at least only partially saturated with water, while the second layer (half-space) is below the water table. The observed Rayleigh wave speed (c_R) satisfies ones expectation based on the observed P-wave and derived S-wave speeds in

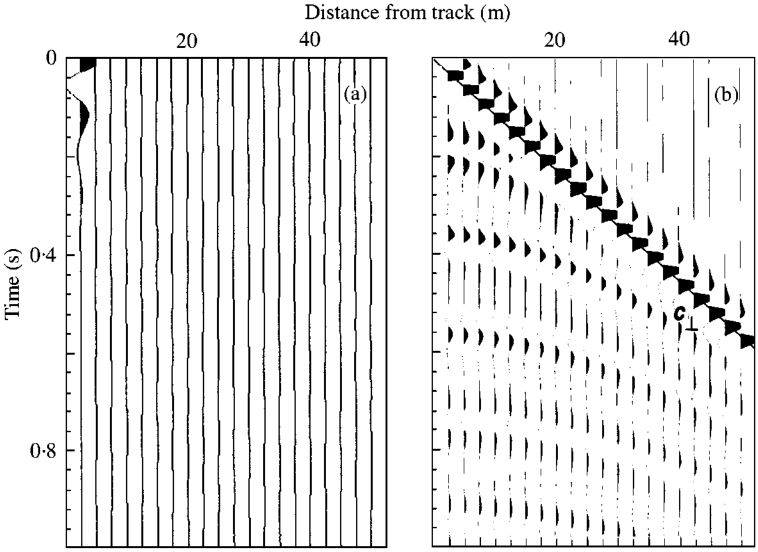

Figure 5. Simulated vertical particle velocity as a function of distance perpendicular to the track and time for (a) subcritical (25 m/s) and (b) supercritical (75 m/s) train speeds. Scale of (b) is 100 times the scale of (a), indicating that the signals in (b) are 100 times stronger. $c_\perp$ is the velocity of the waves propagating perpendicular to the track (about 88 m/s), which is greater than the Rayleigh wave speed (57 m/s).

the top layer with an estimated thickness of about 9·3 m. This thickness can thus be considered as the first boundary in the subsoil.

In order to determine the Lamé coefficients for the soil, assumptions about the densities of the two layers have to be made. The density of the top layer (ρ_1) is taken to be 1800 kg/m^3, corresponding to a clayey soil, and 2000 kg/m^3 in the half-space (ρ_2), corresponding to the density of wet sand.

In Figure 3(b), the simulated response of this one-layer model to an active, non-moving, source has been plotted. A reasonable agreement is noticed, in particular for the two compressional waves and the Rayleigh wave.

Once the soil parameters were determined, several computations have been performed for trains having different speeds, i.e., for a subcritical and a supercritical train speed, and for trains exerting either a constant or an oscillating force. Here, the critical speed has been defined to be the Rayleigh wave speed of a homogeneous half-space with soil properties equal to those of the top layer.

First, the computational results for the case of a non-oscillating load are discussed, for both the subcritical ($c = 25$ m/s) and supercritical case ($c = 75$ m/s). For both cases, the response of the geophones perpendicular to the track is calculated. A bandlimited response is considered, containing frequencies between 2·5 and 60 Hz (with a $\sin^2$ tapering), which is related to the characteristics of the vertical geophones (this is accounted for by the function W of equation (12)).

Figure 5(a) shows the vertical particle velocities at depth $z = 0{\cdot}2$ m, as a function of horizontal distance perpendicular to the track, and as a function of time. It is observed that, for the subcritical case, the generated waves decay very rapidly away from the track. For the supercritical case (see Figure 5(b)), a shock wave is clearly visible, and the vibrational level is much higher in comparison to the subcritical case. In the direction perpendicular to the track, this shock wave propagates with a speed higher than the Rayleigh wave speed:

$$c_\perp = c_R/\sin\theta_r, \tag{14}$$

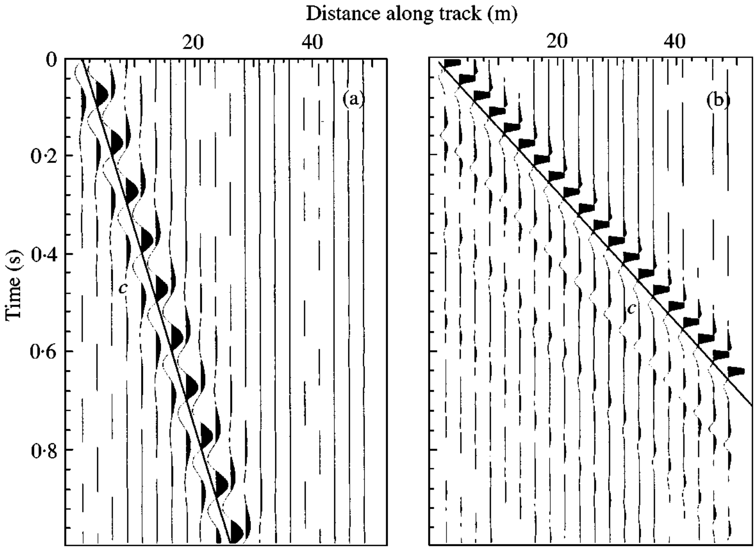

Figure 6. Simulated vertical particle velocity as a function of distance parallel to the track (at a distance of 2·5 m from the track) and time for both (a) subcritical (25 m/s) and (b) supercritical (75 m/s) load speeds. Scale of (b) is 100 times the scale of (a), but equal to the scale in Figure 5(b). The disturbance travels parallel to the track with a velocity equal to the train speed.

where $\theta_R = a\cos(c_R/c)$ (see also reference [1]). In this case, this speed is about 88 m/s. Also visible are multiple reflections of the shock wave at the layer interface at about 9 m depth.

In Figure 6, the velocities computed for the parallel line are plotted as functions of distance along the track, and as functions of time. Here, the distance of the line from the track was 2·5 m. The wave travels with the speed of the train, both for the subcritical (Figure 6(a)) and the supercritical (Figure 6(b)) cases. Again, a stronger vibrational level for trains travelling with supercritical speed is observed.

Now, the experimental results are considered and compared with the modelled results for an oscillating load. In Figure 7, one of the seismograms due to a moving train has been plotted, recorded during the field experiment. Figure 7(a) shows the vertical velocity of the parallel line and Figure 7(b), the velocity of the perpendicular line. In the parallel line record, the waves propagating ahead of the train, in the forward direction, are clearly visible, and the waves propagating backwards are visible when the train has passed. Waves propagating ahead of the train contain higher frequencies than the waves propagating backwards from the train. This is illustrated in the spectra of these two types of waves. In Figure 8, the spectra of two time windows of the measured response data have been plotted. The frequency spectrum of the waves travelling ahead of the train contains higher frequencies and the spectrum of the waves propagating backwards clearly contains lower frequencies, which is due to the Doppler effect.

For a moving source and a stationary observer, it can be shown that

$$\omega_{app} = \omega_c(c_R/(c_R \pm c)), \tag{15}$$

where c_R is the Rayleigh wave speed of the top layer, c is the train velocity, ω_c is the resonant frequency of the train and ω_{app} is the frequency observed by the stationary observer.

First, an attempt is made to estimate the train speed, which was not measured during the experiment. An estimate of the train speed can be obtained by applying equation (15) to two

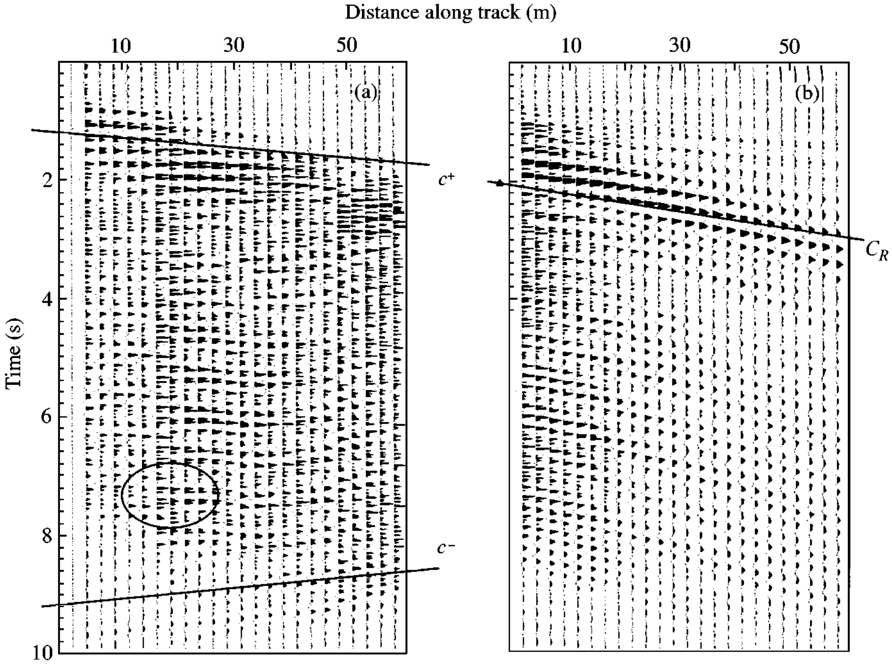

Figure 7. Field measurement of the vertical particle velocity (a) parallel to line and (b) perpendicular to line during a train passage. The train moves from left to right. In (a) forward propagating waves ahead of the train are observed, indicated by c^+, and backward propagating waves, c^- (after the train has passed). In the oval, the transition from forward to backward propagating waves is indicated. Line c_R in (b) indicates the Rayleigh wave, which travels at a speed of 57 m/s.

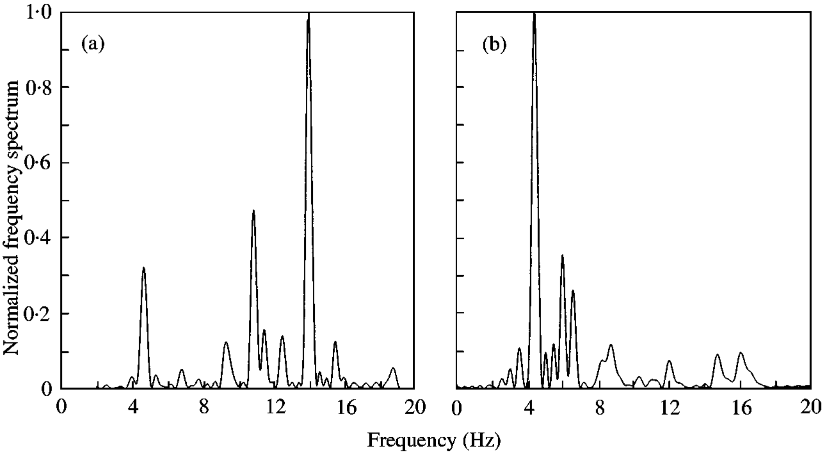

Figure 8. Frequency spectra of the experimental data for (a) forward propagating waves, ahead of the train and (b) backward propagating waves, behind the train.

matching frequency peaks, one in the low-frequency and the other in the high-frequency spectrum. The assumption is made that the frequency of 4·5 Hz in the middle of the spectrum of Figure 8(b) corresponds to the frequency of 11 Hz in the middle of the spectrum of Figure 8(a). In this way, a train speed of about 25 m/s can be found. This value is in agreement with the train speed that is obtained by dividing the distance between axle bogies

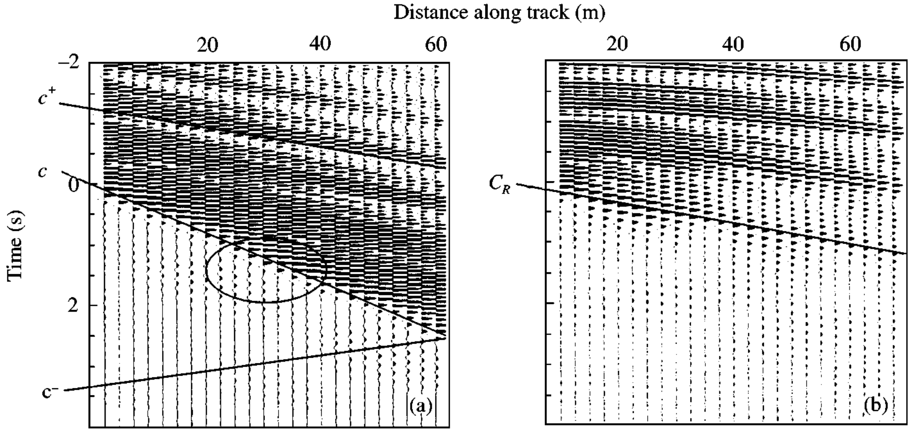

Figure 9. Modelled vertical particle velocity as a function of distance and time, both parallel to the track (a) and perpendicular to the track (b). Train travels at a speed of 25 m/s. Clearly visible are the waves travelling ahead of the train, c^+, and the waves propagating backwards, c^-. The load velocity is indicated by c, which can be retrieved from the transition point from high- to low frequency of each signal, indicated in the oval region. Furthermore, c_R indicates the Rayleigh wave speed.

and the intercept time for sequential arrivals of these bogies. The arrival times can be clearly distinguished in Figure 7(a). Taking a distance between axles of about 18 m, again a train speed of about 25 m/s can be found.

Having determined the train velocity, individual resonance frequencies can be estimated by applying equation (15) on two other coupled frequencies. From the frequencies of 11, 12·6, 14 and 15·5 Hz of Figure 8(a), the values of 6·3, 7·1, 8·0 and 8·8 Hz are obtained for $\omega_c/2\pi$. These frequencies are used as input parameters for the synthetic example, together with the estimate of the train speed. In Figure 9, the simulated response has been plotted. A major difference between the synthetic and real data is the signal length. This is due to the fact that the train is modelled as a single point source, whereas a real train consists of several wheel sets and can be seen as a sequence of point sources, all interacting with each other and thus producing a longer and far more complex signal than the modelled train. However, interesting similarities can be observed if the vertical velocity of the parallel line is considered, for both the real and the synthetic data, shown in Figures 7(a) and 9(a). From the waves propagating ahead of the train, the Rayleigh wave can be clearly distinguished and its velocity can be determined, which corresponds to the earlier found value of 57 m/s. Furthermore, it is observed that waves propagating forward, ahead of the train, contain high frequencies and waves propagating backward, behind the train, contain low frequencies. In the synthetic example, this is more clearly seen than in the real data. Furthermore, in the area of the graph located by the ovals in Figures 7(a) and 9(a), the transition from forward to backward propagating waves can be clearly seen. This transition indicates the moment of the pass-by of the train. In the synthetic example, Figure 9(b), the load speed can be retrieved from these transition points (which are not visible in the real data).

In Figure 10, the Doppler shift can be observed for the simulated train signal, which corresponds to the four main resonance frequencies. The dip in the amplitudes for the low- and high-frequency peaks is due to the bandlimitation $W(\omega)$ of the signal. Both spectra show good agreement with the spectra of the measured data (see Figure 8).

The conclusion can be drawn that there is a good qualitative agreement between the real and the simulated data. Furthermore, it is noticed that vibrations due to an oscillating load

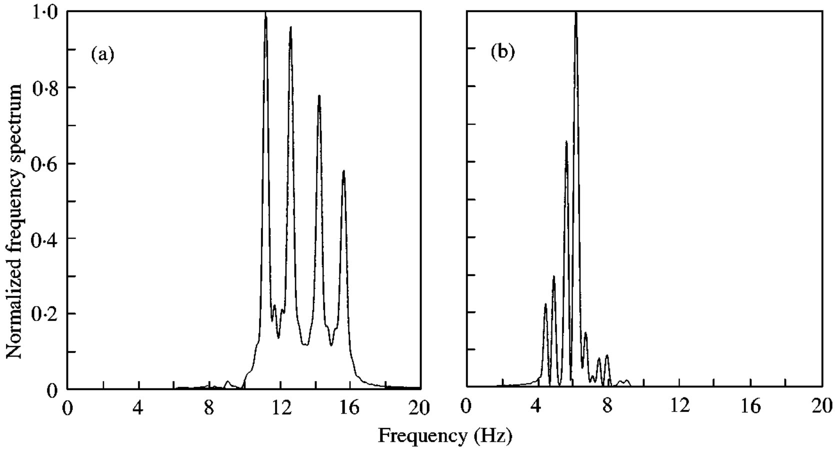

Figure 10. Frequency spectrum of the simulated data for (a) forward propagating waves, ahead of the train and (b) backward propagating waves, behind the train. The decrease in amplitudes of the peaks is due to the bandlimitation of the signal and is due to the modelled characteristics of the geophones and the attenuation parameters.

can be observed at rather large distances, even if the train speed is smaller than the critical wave speed.

4. CONCLUSIONS

In this paper, both theoretical and experimental results have been presented on the vibrations due to moving trains. The theoretical results have been obtained by an efficient, three-dimensional method for the analysis of railway-induced ground vibrations based on a representation of the wavefield in the slowness domain. In this domain, all equations can be expressed in algebraic form for horizontally layered media and can be computed numerically. The experiment has been performed to make a comparison between measurements and theoretical results. The modelled results indicate that, for slow, non-oscillating trains, vibrations decay very rapidly away from the track. However, if the train shows an oscillatory behaviour due to irregularities in the wheels or the track, the vibrations can be observed at larger distances from the track. For trains moving at supercritical speed, shock waves occur. The predictions of the vibrations due to moving trains show a good qualitative agreement with the data of the field experiment. Both the computed and measured results clearly show the Doppler shift and the forward and backward propagating waves. Moreover, the experimental results show that trains generate a significant amount of Rayleigh waves. At the experimental site, the Rayleigh waves propagate with a speed of 57 m/s, which is lower than the intended maximum speed of the high-speed trains in the Netherlands in the near future. In order to compute the quantitative predictions of the vibration level of high-speed trains, a next step is the introduction of the geometry of the embankment into the problem. This scattering problem can be formulated in terms of integral equations employing the Green function that can be determined with the method outlined in the present study.

ACKNOWLEDGMENTS

Helpful discussions with Paul Hölscher of GeoDelft are gratefully acknowledged. The field experiment was performed with the help of a field crew of the Applied Earth Science

Faculty of Delft University of Technology. The crew consisted of Leo de Groot, Albèr Hemstede and Remi Bosch. Their help is greatly appreciated. Finally, the authors acknowledge Ranajit Ghose for his help in the processing and interpretation of the seismograms of the experiment.

REFERENCES

1. V. V. KRYLOV 1996 *Journal of the Acoustical Society of America* **100**, 3121–3134. Vibrational impact of high-speed trains. I. Effect of track dynamics.
2. G. C. HERMAN 1997 *SEG 67th Annual Meeting, Dallas*, Expanded Abstracts, 1913–1916. Waves generated by high-speed trains.
3. J. E. LUCO and R. J. APSEL 1983 *Bulletin of the Seismological Society of America* **73**, 909–929. On the Green's functions for a layered half-space. Part I.
4. F. C. P. DE BARROS and J. E. LUCO 1989 *Wave Motion* **19**, 189–210. Response of a layered viscoealstic half-space to a moving point load.
5. X. SHENG, C. J. C. JONES and M. PETYT 1999 *Journal of Sound and Vibration* **225**, 3–38. Ground vibration generated by a harmonic load acting on a railway track.
6. X. SHENG, C. J. C. JONES and M. PETYT 1999 *Journal of Sound and Vibration* **228**, 129–156. Ground vibration generated by a load moving along a railway track.
7. W. T. THOMSON 1950 *Journal of Applied Physics* **21**, 89–93. Transmission of elastic waves through a stratified soil medium.
8. N. HASKELL 1953 *Bulletin of the Seismological Society of America* **73**, 17–43. The dispersion of surface waves on multilayered media.
9. B. L. N. KENNETT 1983 *Seismic Wave Propagation in Stratified Media*. Cambridge: Cambridge University Press.
10. Ö. YILMAZ 1987 *Society of Exploration Geophysicists*. Seismic data processing.

APPENDIX A: DERIVATION OF THE GREEN SOLUTION

The objective is to obtain a representation for the Green solution in the slowness domain, $\tilde{u}_j^G(p_1, p_2, z)$, which is used in equation (12) to calculate the three components of the displacement vector at the receiver.

The Green solution, in the spatial domain, is the solution of the set of equations, equations (1) and (2), with $f_j(\mathbf{x})$ substituted by $f_j^G(\mathbf{x}; \mathbf{x}') = a_j \delta(\mathbf{x} - \mathbf{x}')$, where $\delta(\mathbf{x} - \mathbf{x}')$ denotes a three-dimensional unit pulse at position $\mathbf{x}'$ and a_j is an arbitrary constant vector. The displacement in the jth direction, observed at position $\mathbf{x}$, is then $u_j^G(\mathbf{x}; \mathbf{x}')$, where the frequency dependence has been omitted because of convenience.

First, it is assumed that the elastic properties are piecewise constant in each layer. Then, coupled equations for displacement and stress can be set-up, in which the dependence on the vertical co-ordinate is emphasized.

The displacement and the traction are both continuous across any horizontal plane in the medium. Therefore, the equations of motion and the constitutive relation are reorganized, thus generating a system of first order differential equations with respect to depth z. Two decoupled sets of equations are obtained, after the introduction of some new elements:

$$u_V^G = \partial_1 u_1^G + \partial_2 u_2^G, \qquad u_H^G = \partial_1 u_2^G - \partial_2 u_1^G. \tag{A.1, A.2}$$

For both the stresses τ_{V3}^G, τ_{H3}^G and the forces f_V, f_H, a similar procedure can be applied. The vertical components, u_3^G, τ_{33}^G and f_3^G, remain unchanged. The decoupling is in terms of the compressional and vertically polarized shear waves and the horizontally polarized shear waves.

A.1. DECOUPLING: P–SV AND SH SYSTEMS

Both sets of equations have the form

$$\partial_3 \mathbf{b} = \omega \mathbf{A}_n \mathbf{b} - \mathbf{s}, \tag{A.3}$$

where the subscript n denotes the layer number.

For P–SV waves, the equation reads as

$$\partial_3 \begin{bmatrix} U \\ V \\ P \\ S \end{bmatrix} = \omega \begin{bmatrix} 0 & p\left(1 - \dfrac{2\beta_n^2}{\alpha_n^2}\right) & (\rho_n \alpha_n^2)^{-1} & 0 \\ -p & 0 & 0 & (\rho_n \beta_n^2)^{-1} \\ -\rho_n & 0 & 0 & p \\ 0 & \rho_n(\upsilon_n p^2 - 1) & -p\left(1 - \dfrac{2\beta_n^2}{\alpha_n^2}\right) & 0 \end{bmatrix} \begin{bmatrix} U \\ V \\ P \\ S \end{bmatrix} - \begin{bmatrix} 0 \\ 0 \\ F_3 \\ F_V \end{bmatrix}, \tag{A.4}$$

where $p = \sqrt{(p_1^2 + p_2^2)}$ and $z_{n-1} < z < z_n$ and for SH waves, the following equation is obtained:

$$\partial_3 \begin{bmatrix} W \\ T \end{bmatrix} = \omega \begin{bmatrix} 0 & (\rho_n \beta_n^2)^{-1} \\ \rho_n(\beta_n^2 p^2 - 1) & 0 \end{bmatrix} \begin{bmatrix} W \\ T \end{bmatrix} - \begin{bmatrix} 0 \\ F_H \end{bmatrix}. \tag{A.5}$$

In equation (A.4) and (A.5), U, V, W, P, S, T and F_3, F_V, F_H are scaled variables. They read as

$$U = \tilde{u}_3^G, \quad P = \tilde{\tau}_{33}^G/\omega, \quad F_3 = \tilde{f}_3^G/\omega, \quad V = -\,\tilde{u}_H^G/(\omega p), \quad S = -\,\tilde{\tau}_{V3}^G/(\omega^2 p),$$

$$F_V = -\tilde{f}_V^G/(\omega^2 p), \quad W = -\,\tilde{u}_H^G/(\omega p), \quad T = -\,\tilde{\tau}_{H3}^G/(\omega^2 p), \quad F_H = -\tilde{f}_H^G/(\omega^2 p). \tag{A.6}$$

Equations (A.4) and (A.5) are similar to the ones presented by Kennett [9, pp. 29–30], the only difference being the fact that, instead of the radial p of Kennett, here slowness $p = \sqrt{p_1^2 + p_2^2}$ is obtained. Thus, a similar approach can be followed to determine the response of a layered half-space in the slowness domain. In the subsequent sections, all expressions necessary for the computations are presented. For certain aspects of the derivations the reader is referred to reference [9].

A.2. SCATTERING MATRIX METHOD

The first order differential equations, derived in the previous section, are solved by using a recursive method, called the scattering matrix method. The main advantage of the recursive solution method is that it reduces the effect of exponentially growing terms and therefore it can handle thick layers and evanescent waves properly. A propagator approach can become less effective in these cases.

A.2.1. *Up- and downgoing waves*

The boundary value problem, equation (A.3), is solved by computing the scattering matrices of the region above the source and the region below the source. The scattering matrix of a section between two reference levels describes the relation between waves propagating towards that section and propagating away from that section. The scattering matrices of the sections are constructed recursively, and contain the transmission and reflection properties of each of the interfaces present.

To find a relation between the waves above and below the source level, a transformation of the field into up- and downgoing waves is performed. This can be done by multiplying equation (A.3) with $\mathbf{D}_n^{-1}$, the inverse eigenvector matrix of $\mathbf{A}_n$. The solution of the resulting equation reads as

$$\mathbf{v}(z) = \mathbf{Q}_n(z, \tilde{z})\mathbf{v}(\tilde{z}) \quad \text{with } z_{n-1} < \tilde{z}, \quad z < z_n \tag{A.7}$$

in terms of a wave propagator $\mathbf{Q}_n$ $(= \mathrm{e}^{\mathrm{j}\omega(z-\tilde{z})}\mathbf{\Lambda}_n\mathbf{v}(\tilde{z}))$, which depends on the difference between the observation and reference depth. Matrix $\mathbf{\Lambda}_n$ is the eigenvalue matrix of $\mathbf{A}_n$, and $\mathbf{v} = \mathbf{D}_n^{-1}\mathbf{b}$ is the vector consisting of up- and downgoing-wave components.

For P–SV waves, matrix $\mathbf{Q}_n$ reads as

$$\mathbf{Q}_n(z, \tilde{z}) = \mathrm{diag}(\mathrm{e}^{-\mathrm{j}\omega q_{\alpha,n}(z-\tilde{z})}, \mathrm{e}^{-\mathrm{j}\omega q_{\beta,n}(z-\tilde{z})}, \mathrm{e}^{\mathrm{j}\omega q_{\alpha,n}(z-\tilde{z})}, \mathrm{e}^{\mathrm{j}\omega q_{\beta,n}(z-\tilde{z})})$$

$$\text{with } z_{n-1} < \tilde{z}, \quad z < z_n \tag{A.8}$$

and for SH waves

$$\mathbf{Q}_n(z, \tilde{z}) = \mathrm{diag}(\mathrm{e}^{-\mathrm{j}\omega q_{\beta,n}(z-\tilde{z})}, \mathrm{e}^{\mathrm{j}\omega q_{\beta,n}(z-\tilde{z})} \quad \text{with } z_{n-1} < \tilde{z}, \quad z < z_n) \tag{A.9}$$

with $q_{\{\alpha,\beta\},n} = \sqrt{1/\{\alpha, \beta\}_n^2 - p^2}$ denoting the vertical slowness for the nth layer.

A.3. WAVEFIELD AT SOURCE LEVEL

The wavefield at the receiver level can be determined by calculating the wavefield at the source level and subsequently propagating the wavefield to the receiver. The wavefield at the source can be expressed in terms of discontinuities. In terms of up- and downgoing waves, explicit expressions are obtained for both the downgoing wavefield just below the source level z_{src}, i.e., $\mathbf{v}_D(z_{src}^+)$, and the upgoing wavefield just above the source, i.e., $\mathbf{v}_U(z_{src}^-)$. They read as

$$\mathbf{v}_D(z_{src}^+) = (\mathbf{I} - \mathbf{S}_U^{src}\mathbf{S}_D^{src})^{-1}(\sigma_D - \mathbf{S}_U^{src}\sigma_U), \tag{A.10}$$

$$\mathbf{v}_U(z_{src}^-) = (\mathbf{I} - \mathbf{S}_D^{src}\mathbf{S}_U^{src})^{-1}(\mathbf{S}_D^{src}\sigma_D - \sigma_U), \tag{A.11}$$

where σ_U and σ_D are the source discontinuities, expressed in up- and downgoing waves, with the source assumed to be located in the n_sth layer. Vector σ is then defined as follows:

$$\sigma = (\sigma_U^{\mathrm{T}}, \sigma_D^{\mathrm{T}})^{\mathrm{T}} = \mathbf{D}_{n_s}^{-1}\mathbf{s}, \tag{A.12}$$

where $\mathbf{D}_{n_s}^{-1}$ is the inverse of the local eigenvector matrix of the source layer and $\mathbf{s}$ follows from equation (A.3)–(A.5).

Matrices $\mathbf{S}_U^{src}$ and $\mathbf{S}_D^{src}$, appearing in equation (A.10) and (A.11), are the scattering matrices for the sections above and below the source respectively. They are constructed according to a recursive scheme. The scattering matrices for the upgoing and downgoing waves are given by

$$\mathbf{S}_U^{src} = \mathbf{E}_U^{src}\mathbf{S}_U^{n_s-1}\mathbf{E}_U^{src} \tag{A.13}$$

and

$$\mathbf{S}_D^{src} = \mathbf{E}_D^{src}\mathbf{S}_D^{n_s}\mathbf{E}_D^{src}. \tag{A.14}$$

Here, $\mathbf{S}_U^{n_s-1}$ is the scattering matrix for the section above the $(n_s - 1)$th interface. $\mathbf{S}_D^{n_s}$ is the scattering matrix for the section beneath the n_sth interface. $\mathbf{E}_U^{src}$ and $\mathbf{E}_D^{src}$ are the propagation matrices from the source to interfaces above and beneath the source respectively. They can be retrieved from the wave propagator $\mathbf{Q}_n$ (see equations (A.8) and (A.9)).

Matrices $\mathbf{S}_U^{n_s-1}$ and $\mathbf{S}_D^{n_s}$ can be constructed with the help of a recursive scheme. For $\mathbf{S}_U^{n_s-1}$ the scheme reads as

$$\mathbf{S}_U^n = \begin{cases} \mathbf{R}_U^0 & \text{for } n = 0 \\ \mathbf{R}_U^n + \mathbf{T}_D^n\mathbf{E}^n\mathbf{S}_U^{n-1}\mathbf{E}^n(\mathbf{I} - \mathbf{R}_D^n\mathbf{E}^n\mathbf{S}_U^{n-1}\mathbf{E}^n)^{-1}\mathbf{T}_U^n & \text{for } n > 0. \end{cases} \tag{A.15}$$

The recursion starts with $n = 0$ and ends as soon as $n = n_s - 1$ has been reached. The scattering matrix $\mathbf{S}_U^n(n > 0)$ is a sum of a part, describing the reflection at the nth interface and a part which describes the transmission upwards through the nth interface, the generation of multiples, the reflection of these waves by the previous scattering matrix and the transmission downwards through the nth interface [9, p. 133]. Equation (A.15) holds for both the P–SV and the SH systems. For $n = 0$, the scattering matrix of the upgoing waves is equal to the reflection of the free surface, because no transmission takes place through this interface and no waves enter the half-space. Therefore, $\mathbf{S}_U^0 = \mathbf{R}_U^0$, where $\mathbf{R}_U^0$ is given in equation (C.2) for P–SV waves and in equation (C.3) for SH waves. Detailed expressions of the reflection and transmission matrices for interfaces are given in Appendix C. In equation (A.15) matrix $\mathbf{E}^n$ describes the propagation of waves in the nth layer.

The derivation of matrix $\mathbf{S}_D^{n_s}$ is similar to the derivation of $\mathbf{S}_U^{n_s-1}$ and the reader is referred to reference [9]. The use of such a recursive scheme reduces the effect of exponentially growing terms and thus handles thick layers and evanescent waves more accurately.

A.4. WAVEFIELD AT RECEIVER LEVEL

After computation of the wavefield at the source level, the wavefield at the receiver can be calculated by propagating the field from source to receiver level. Assuming that the receiver and source are located in the same layer, the wavefield at the receiver level is now obtained from

$$\mathbf{v}(z_r) = \mathbf{Q}_{n_s}(z_r, z_s)\mathbf{v}(z_s) \tag{A.16}$$

with $\mathbf{Q}_{n_s}(z_r, z_s)$ the wave propagator, given in equations (A.8) and (A.9).

The case of the receiver and source being located in different layers will not be discussed here, but the reader is referred to Kennett [9, pp. 163–170].

A.5. GREEN SOLUTION

Finally, the wavefield at the receiver level in terms of U, V and W is obtained by multiplying the wavefield vector $\mathbf{v}$ with the eigenvector matrix $\mathbf{D}_n$. The Green solution in the slowness domain then reads as

$$\begin{bmatrix} \tilde{u}_1^G \\ \tilde{u}_2^G \\ \tilde{u}_3^G \end{bmatrix} = \frac{1}{p} \begin{bmatrix} 0 & jp_1 & -jp_2 \\ 0 & jp_2 & jp_1 \\ p & 0 & 0 \end{bmatrix} \begin{bmatrix} U \\ V \\ W \end{bmatrix}, \tag{A.17}$$

where equations (A.1), (A.2) and (A.6) have been used.

APPENDIX B: EIGENVECTOR MATRIX **D**

In this appendix, expressions for eigenvector matrix $\mathbf{D}_n$ and its inverse $\mathbf{D}_n^{-1}$ are presented. They have been derived by Kennett [9, pp. 48–51].

The eigenvector matrix has the form

$$\mathbf{D}_n = \begin{bmatrix} \mathbf{M}_{U,n} & \mathbf{M}_{D,n} \\ \mathbf{N}_{U,n} & \mathbf{N}_{D,n} \end{bmatrix} \tag{B.1}$$

for both types of waves. For P–SV waves it consists of the following 2×2 matrices:

$$\mathbf{M}_{\{U,D\},n} = \begin{bmatrix} \mp \varepsilon_{\alpha,n} j q_{\alpha,n} & \varepsilon_{\beta,n} p \\ \varepsilon_{\alpha,n} p & \mp \varepsilon_{\beta,n} j q_{\beta,n} \end{bmatrix}, \tag{B.2}$$

$$\mathbf{N}_{\{U,D\},n} = \begin{bmatrix} \varepsilon_{\alpha,n} \rho_n (2\beta_n^2 p^2 - 1) & \mp \varepsilon_{\beta,n} 2j\rho_n \beta_n^2 p q_{\beta,n} \\ \mp \varepsilon_{\alpha,n} 2j\rho_n \beta_n^2 p q_{\alpha,n} & \varepsilon_{\beta,n} \rho_n (2\beta_n^2 p^2 - 1) \end{bmatrix} \tag{B.3}$$

with $\varepsilon_{\alpha,n} = (2\rho_n q_{\alpha,n})^{-1/2}$ and $\varepsilon_{\beta,n} = (2\rho_n q_{\beta,n})^{-1/2}$. For SH waves, the elements read as

$$\mathbf{M}_{\{U,D\},n} = \varepsilon_{\beta,n}/\beta_n, \qquad \mathbf{N}_{\{U,D\},n} = \mp \varepsilon_{\beta,n} j \rho_n \beta_n q_{\beta,n}. \tag{B.4, B.5}$$

The inverse eigenvector matrix reads as

$$\mathbf{D}_n^{-1} = \mathrm{j} \begin{bmatrix} -\mathbf{N}_{D,n}^{\mathrm{T}} & \mathbf{M}_{D,n}^{\mathrm{T}} \\ \mathbf{N}_{U,n}^{\mathrm{T}} & -\mathbf{M}_{U,n}^{\mathrm{T}} \end{bmatrix}. \tag{B.6}$$

APPENDIX C: REFLECTION AND TRANSMISSION MATRICES

C.1. REFLECTION AT THE FREE SURFACE

In reference [9, p. 118], expressions for the reflection matrices at the free surface for both P–SV and SH waves can be found. For both systems, the following relation holds:

$$\mathbf{R}_U^0 = -\mathbf{N}_{D,1}^{-1} \mathbf{N}_{U,1}. \tag{C.1}$$

For P–SV waves the reflection matrix then reads as

$$\mathbf{R}_U^0 = \frac{1}{4p^2 q_{\alpha,1} q_{\beta,1} + v_1^2} \begin{bmatrix} 4p^2 q_{\alpha,1} q_{\beta,1} - v_1^2 & 4ipv\sqrt{q_{\alpha,1} q_{\beta,1}} \\ 4ipv_1\sqrt{q_{\alpha,1} q_{\beta,1}} & 4p^2 q_{\alpha,1} q_{\beta,1} - v_1^2 \end{bmatrix} \tag{C.2}$$

with $v_1 = 2p^2 - 1/\beta_1^2$.

For *SH* waves the reflection scalar reads as

$$\mathbf{R}_U^0 = 1. \tag{C.3}$$

C.2. REFLECTION AND TRANSMISSION AT AN INTERFACE

The transmission and reflection matrices at an interface read as

$$\mathbf{T}^n_{\{U,D\}} = j\langle \mathbf{M}_{D,n}, \mathbf{M}_{\{U,D\},n+1}\rangle^{-1}, \tag{C.4}$$

$$\mathbf{R}^n_{\{U,D\}} = -\langle \mathbf{M}_{\{U,D\},n}, \mathbf{M}_{D,n+1}\rangle^{-1}\langle \mathbf{M}_{U,n}, \mathbf{M}_{\{U,D\},n+1}\rangle, \tag{C.5}$$

where the $\langle\ \rangle$ operation in equation (C.4) is defined by

$$\langle \mathbf{M}_{D,n}, \mathbf{M}_{U,n+1}\rangle = (\mathbf{M}_{D,n})^{\mathrm{T}}\mathbf{N}_{U,n+1} - (\mathbf{N}_{D,n})^{\mathrm{T}}\mathbf{M}_{U,n+1}. \tag{C.6}$$